Journal of Materials Chemistry A

Accepted Manuscript

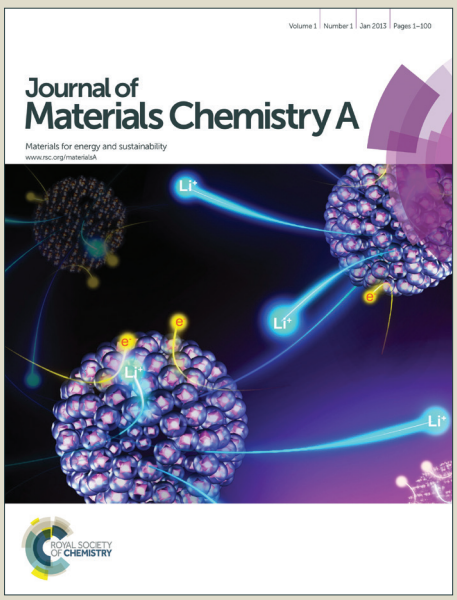

ROYAL SOCIETY OF CHEMISTRY

www.rsc.org/materialsA

Cite this: DOI: 10.1039/c0xx00000x

www.rsc.org/xxxxxx

ARTICLE TYPE

Hierarchical nanosheet-based $NiMoO_4$ nanotubes: Synthesis and high supercapacitor performance†

Zhuoxun Yin,[a] Shen Zhang,[a] Yujin Chen,*[a] Peng Gao,*[b] Chunling Zhu,[b] Piaoping Yang*[b] and Lihong Qi[a]

Received (in XXX, XXX) Xth XXXXXXXXX 20XX, Accepted Xth XXXXXXXXX 20XX

DOI: 10.1039/b000000x

Hierarchical nanosheet-based $NiMoO_4$ nanotubes were synthesized by a hydrothermal treatment and subsequent an in situ diffusion reaction method. The naotubes with a high surface area of 128.5 m^2 g^{-1} were composed of highly ordered ultrathin nanosheets with a thickness of less than 10 nm. As used as electrodes in electrochemical capacitors, the hierarchical nanotubes exhibited excellent electrochemical performances. The specific capacitance of the hierarchical nanotubes was up to 864 F g^{-1} at a current density of 1 A g^{-1}. The results indicate that the hierarchical nanosheet-based $NiMoO_4$ nanotubes are very promising for applications in energy storage and other electrochemical devices. Furthermore, the strategy presented here is facile, and may be expended as a typical method to synthesize other kinds of metal molybdate nanotubes.

1 Introduction

Metal (Fe, Co, Ni, and Mn) molybdates, important families of inorganic materials, have promising applications in many fields, such as catalysts,[1-11] humidity and gas sensors,[12-14] energy storage devices,[15-23] and so forth. In order to improve their physicochemical properties, researchers have developed several approaches in the past few years, including solid-state reactions, coprecipitation, hydrothermal and sol−gel methods, to fabricate various metal molybdate nanostructures. As a result, metal molybdate nanoparticles,[9] nanorods,[12, 13, 15, 18] nanowires,[24, 25] and nanotubes [5] have been successfully synthesized. However, to the best of our knowledge, the synthesis of hierarchical nanosheet-based $NiMoO_4$ nanotubes with a high surface area has not been reported.

Electrochemical supercapacitors (ECs) with properties intermediate to those of batteries and electrostatic capacitors have attracted more and more attention due to their pulse power density supply, fast charging, and excellent cycling stability, which play an important role in power-source applications such as short-term power sources and hybrid electric vehicles.[26-29] In general, in terms of charge/discharge mechanism, electrochemical supercapacitors can be classified into categories: electrical double-layer capacitors (EDLCs) and Faradaic pesudocapacitors. Compared with EDLCs, Faradaic pesudocapacitors exhibit higher specific capacitance and energy density because they can provide a variety of oxidation states for efficient redox reactions. Metal molybdate nanostrucutures as electrode materials of ECs have been extensively investigated due to their peseudocapacitive behaviors.[15-21] Mai et al reported that hierarchical $MnMoO_4$/$CoMoO_4$ heterostructured nanowires exhibited a specific capacitance of 187.1 F g^{-1} at a current density of 1 A g^{-1} and good reversibility with a cycling efficiency of 98% after 1,000 cycles.[15] Liu et al demonstrated that $CoMoO_4$ nanorods had a high capacitance of 286 F g^{-1} at a current density of 5 mA cm^{-2} and 97.5 % of the initial capacitance was remained after 2000 cycles. [16] Xia et al fabricated $CoMoO_4$/graphene composites through a hydrothermal method, and the composites showed a specific capacitance of 394.5 F g^{-1} at a scan rate of 1 mV s^{-1}.[17] The specific capacitance of $CoMoO_4$/carbon naotube composites was about 170 F g^{-1} at a current density of 0.1 A g^{-1} under an optimal experimental condition.[21] Plate-like $CoMoO_4$ nanostructures exhibiting a maximum specific capacitance of about 133 F g^{-1} at a current density of 1 mA cm^{-2} were also demonstrated.[20] Nevertheless, compared with RuO_2-based materials these metal molybdate nanostructures had relatively low specific capacitances.[30, 31]

As reported, metal molybdates with large surface and highly ordered structure would exhibit excellent electrochemical performance.[15] Herein, we developed a facile method based on an in situ diffusion reaction growth method to fabricate hierarchical nanosheet-based $NiMoO_4$ nanotubes with a surface area of as high as 128.5 m^2 g^{-1}. Applied as the electrode of ECs, the material exhibited a specific capacitance of 864 F g^{-1} at a current density of 1 A g^{-1}, and good stability with a 71 % of the initial capacitance remained after 1000 cycles.

2 Experimental Section

2.1 Synthesis of hierarchical nanosheet-based $NiMoO_4$ nanotubes

The synthesis of hierarchical nanosheet-based $NiMoO_4$ nanotubes was included a two-step process. 0.075 g of MoO_3 nanorods [32-34] was dispersed in 35 mL of water/ethanol (volume ratio = 1:1) solvent containing 0.618 g of nickel acetate under stirring for 10 min. The mixture above was then transferred into a Teflon-lined

stainless steel autoclave with a capacity of 50 mL for hydrothermal treatment at 90°C for 5 h. As the autoclave cooled to room temperature naturally, the precipitates were separated by centrifugation, washed with distilled water and absolute ethanol, and dried in air. The products above, named as $NiMoO_4$ precursors for convenience, were annealed at air atmosphere at 500°C for 4 h, and then hierarchical nanosheet-based $NiMoO_4$ nanotubes were then obtained.

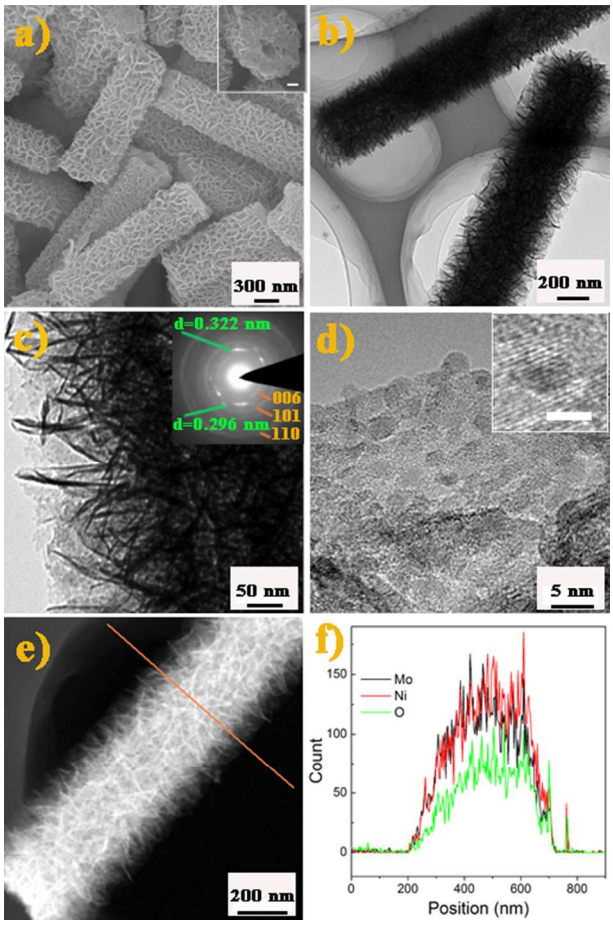

Fig. 1 Structural characterization of the 3D precursors. a) SEM image, the inset showing the hollow characteristic of the 3D precursors, the scale bar: 100 nm, b, c) TEM images, the inset showing SAED pattern, d) HRTEM image, the scale bar in the inset: 2 nm, e) ADF STEM image, and f) Line-scan EELS.

2.2 Characterization

The morphology and size of the synthesized samples were characterized by scanning electron microscope (HITACHI S−5200) and transmission electron microscope (FEI Tecnai-F20) equipped with a Gatan imaging filter (GIF). The crystal structure of the sample was determined by X-ray diffraction (XRD) [D/max 2550 V, Cu Kα radiation]. X−ray photoelectron spectroscopy (XPS) measurements were carried out using a spectrometer with Al Kα radiation (Thermo Scientific K-Alpha). The pore diameter distribution and surface area were tested by nitrogen adsorption/desorption analysis (TRISTAR II3020).

2.3 Electrochemical measurements

A three electrodes consisting of nickel foam as working electrode ($1cm^2$), Pt foil and a saturated calomel electrode (SCE) as counter and reference electrodes were used. Cyclic voltammetry and galvanostatic charge-discharge curves were carried out using a CHI 660D electrochemical workstation. KOH (2.0 M) was used as the electrolyte. The working electrode consisted of 75 wt% of the active material, 15 wt% of acetylene black, and 10 wt% of polytetrafluoroethylene. The loading weight of active $NiMoO_4$ is around 7 mg.

3 Results and discussion

The SEM and TEM images show that the diameter and length of MoO_3 nanorods with a single crystal nature obtained by a hydrothermal method are about 170 nm and several micrometers, respectively (Fig.S1, Electronic Supplementary Information (ESI)). † The hiearchical $NiMoO_4$ precursors can be obtained after MoO_3 nanorods are hydrotheramlly treated in the nickel acetate solution containing water and ethanol at 90°C for 5 h. XRD analysis shows that the $NiMoO_4$ precursors contains $Ni(OH)_2{\cdot}0.75H_2O$ (JCPDS, no. 38−0715), α-MoO_3 (JCPDS, no. 35−0609), and $NiMoO_4{\cdot}xH_2O$ (JCPDS, no. 13−0128), as shown in Fig. S2. † XPS measurements (Fig. S3) further confirm that the precursors contain Mo, Ni, and O elements. The atomic ratio of Mo to Ni determined by XPS is about 1.27:1. †

The morphology and the structure of the $NiMoO_4$ precursors were investigated by scanning electron microscopy (SEM) and transmission electron microscopy (TEM) analyses. Interestingly, many nanosheets are almost grown perpendicularly on the surface of 1D MoO_3 nanostructures, forming an interesting three-dimensional (3D) hierarchical architecture, as shown in Fig. 1(a) and 1(b). It is also clearly found that the average diameter of the 3D hierarchical nanostructures (about 500 nm) is great increased, in comparison with the pristine MoO_3 nanorods (about 170 nm), [32-34] while their lengths (about 2.5 μm) are decreased significantly which may result from the alkali etching. The inset in Fig. 1(a) indicates that the central parts of the 1D MoO_3 nanostructures are hollow due to the alkali etching. TEM image (Fig. 1(b) and 1(c)) shows that the nanosheets in the $NiMoO_4$ precursors have a thickness of less than 10 nm, and their height is about 150 nm. Fig. 1(d) is a typical TEM image of the basal plane of the nanosheets. It can be clearly found that many small particles are anchored on the surfaces of the nanosheets. The lattice fringes in the corresponding high-resolution TEM (HRTEM) image reveals that the small particles are of a crystal nature. The diffraction rings marked by yellow lines in the selected-area electron diffraction (SAED) of the basal plane of the nanosheets (the inset in Fig. 1(c) correspond to (006), (101) and (110) crystalline planes of $Ni(OH)_2{\cdot}0.75H_2O$, respectively, whereas the diffraction dots marked by the green lines correspond to the crystalline planes of $NiMoO_4{\cdot}xH_2O$ with the lattice distances of 0.322 and 0.296 nm, respectively. In order to determine the phases of the nanosheets and the nanoparticles, an additional experiment was carried out, in which the experimental condition was kept the same one that was used to synthesize 3D hierarchical nanostructures except that MoO_3 nanorods were not added in the reaction system. After the hydrothermal treatment at 90°C for 5 h, the sheet-like products were obtained (Fig. S4). † Thus, the nanosheets are $Ni(OH)_2{\cdot}0.75H_2O$, while the nanoparticles anchored on their surfaces are $NiMoO_4{\cdot}xH_2O$. To further determine the distribution of the elements in the 3D hierarchical

nanostructures, an annular dark-field (ADF) scanning transmission electron microscopy (STEM, Fig. 1(e)) and line-scan electron energy loss spectroscopy (EELS, Fig. 1(f)) were carried out. As shown in Fig. 1(f), the Mo, Ni, and O elements distribute uniformly in the whole regions of the 3D hierarchical nanostructures, which further confirms the SEAD and TEM results.

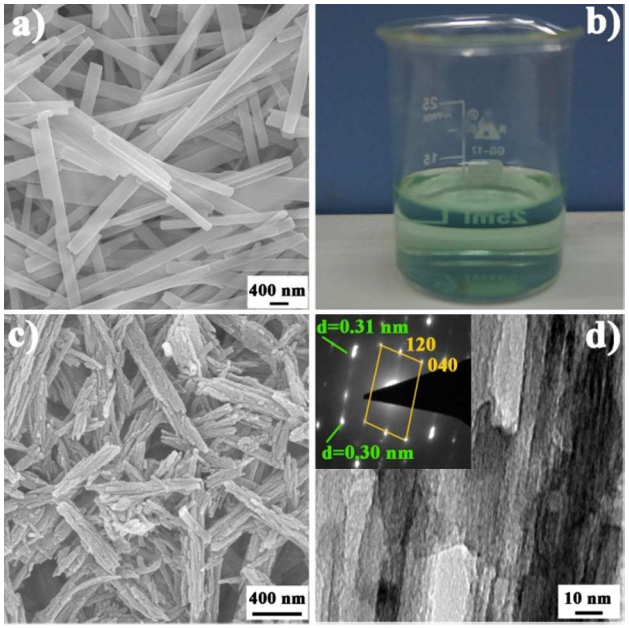

Fig. 2 a) SEM images of the products obtained in the ethanol system, b) **Photograph** of the solution obtained in the water system, **and c) SEM and d) TEM images of the precipitate as the solution aged for above 4 h, respectively. The inset in d) showing the corresponding SAED pattern of the precipitate as the solution aged for above 4 h.**

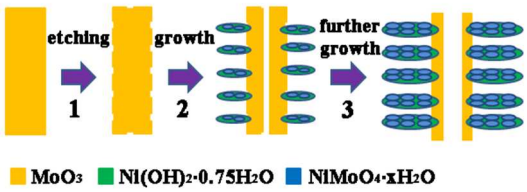

Scheme 1 Schematic illustration showing the growth mechanism of the 3D precursors.

In the terms of the analyses above, an interesting 3D nanostructures, i.e., $Ni(OH)_2 \cdot 0.75H_2O$ nanosheets with small nanoparticles anchored on their surfaces perpendicularly grown on the surfaces of 1D hollow MoO_3 nanostructures. The further experimental results show that the volume ratio of ethanol to water plays a very important role in the formation of the interesting 3D nanostructures. In the ethanol system any materials was not grown on the surfaces of the MoO_3 nanorods (Fig. 2(a)), whereas in the water system the MoO_3 nanorods would almost be etched totally and relatively transparent solution was obtained as the the autoclave cooled to room temperature initially (Fig. 2(b)). However, after the solution aged for above 4 h at room temperature, small amount of precipitate was formed in the bottom of the solution. The formation of the precipitate taking a period of time may be attributed to its low density. XRD analysis (Fig. S5) reveals that the precipitate consists of crystalline $NiMoO_4 \cdot xH_2O$, MoO_3, and $NiMoO_4$† SEM image (Fig. 2(c)) shows that the precipitate exhibits a rod-like morphology with porous characteristic. The porous characteristic is further conformed by TEM observation, as shown in Fig. 2(d). The diffractin dots marked by the green lines in SAED pattern (the inset in Fig. 2(d)) marked by the green lines can be indexed to the planes of $NiMoO_4 \cdot xH_2O$ with the lattice distance of 0.31 and 0.30 nm, respectively. In the pattern, the diffraction dots marked by the yellow lines can be attributed to orthorhombic MoO_3, in which the marked dots correspond to (120) and (040) planes of MoO_3.

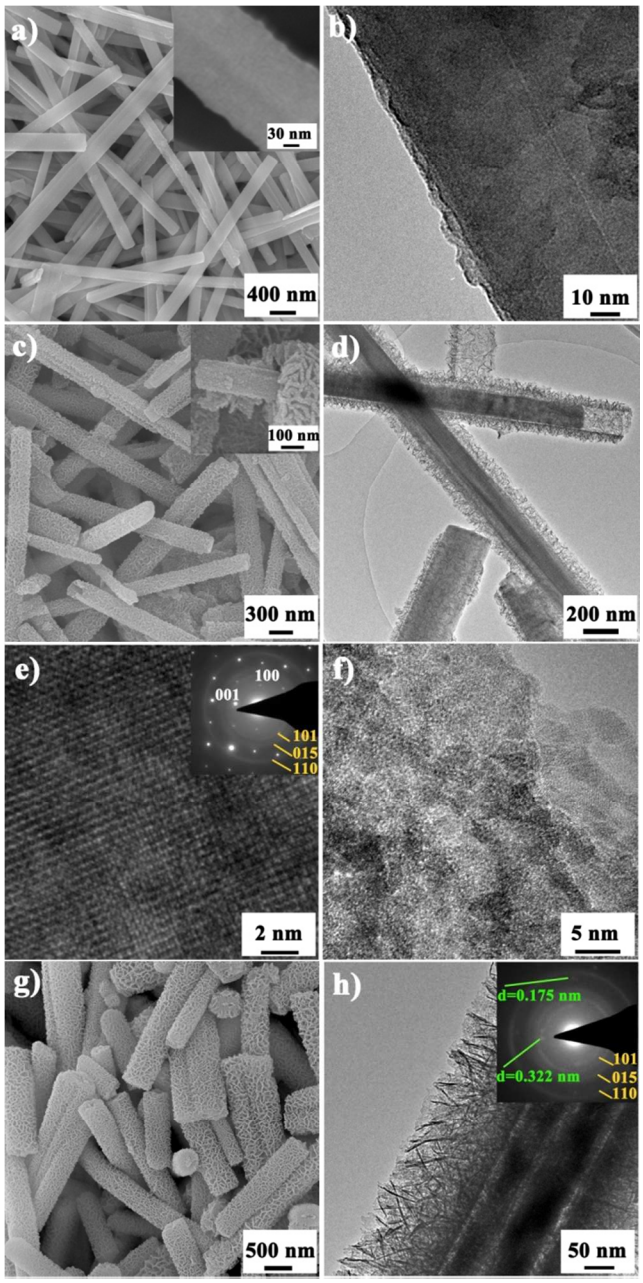

Fig. 3 The structural characterization of the products obtained at different reaction stage. (a) SEM and (b) TEM images (70°C for 10 min), (c) SEM, (d) TEM, (e) HRTEM and (f) HRTEM images (90°C for 10 min), (g) SEM and TEM images (90°C for 2 h).

$$CH_3COO^- + H_2O \rightarrow CH_3COOH + OH^- \quad (1)$$

$$MoO_3 + 2OH^- \rightarrow MoO_4^{2-} + H_2O \quad (2)$$

$$OH^- + Ni^{2+} \rightarrow Ni(OH)_2 \quad (3)$$

$$MoO_4^{2-} + Ni^{2+} \rightarrow NiMoO_4 \quad (4)$$

In terms of the experimental results above, we proposed a mechanism for the growth of the interesting 3D nanostructures, which illustrated in Scheme 1. OH^- ions produced after the hydrolysis of nickel acetate (Equation 1) etch MoO_3 nanorods, leading to the formation of defect sites on the surfaces of MoO_3 nanorods, as shown in step1 in Scheme 1. This is evidenced by SEM and TEM images of the product obtained at 70°C for 10 min, as shown in Fig. 3(a) and (b). XRD measurement (Fig. S6(a)) shows the product obtained at the stage is still crystaline MoO_3. † The defects can serve as active nucleation sites for subsequent growth of $Ni(OH)_2{\cdot}0.75H_2O$ nanosheets (Equation 1) on the surfaces of the MoO_3 nanorods (Equation 3), as shown in step 2 in Scheme 1. During this step, small $NiMoO_4{\cdot}xH_2O$ nanoparticles are also formed (Equations 2 and 4), and deposited on the surfaces of $Ni(OH)_2{\cdot}0.75H_2O$ nanosheets. Due to the presence of $Ni(OH)_2{\cdot}0.75H_2O$ nanosheets on their surfaces, the weak alkali etching occurs more easily along axial direction of the MoO_3 nanorods, which results in void spaces in the axial direction of the MoO_3 nanorods. In order to clarify the processes, we characterized the structures of the products obtained at 90°C for 10 min and 2 h. Fig. 3(c) and (d) show SEM and TEM images of the product obtained at 90°C for 10 min. It can be clearly found that sheet-like materials with a height of 85 nm were grown on the surface of MoO_3. A high-magnification SEM image shows that there are some MoO_3 nanorods with uncoated tips. HRTEM image taken from uncoated tips of MoO_3 nanorods reveals crystal structure of the nanorods keep undamaged at the reaction stage, as shown in Fig. 3(e). The diffraction dots in the SAED pattern (the inset in Fig. 3 (e)) come from orthorhombic MoO_3, in which the marked ones correspond to (001) and (100) planes of MoO_3. In addition, the diffraction rings, marked by the yellow lines, can be indexed to (101), (015) and (110) planes of $Ni(OH)_2{\cdot}0.75H_2O$. It demonstrates that the sheet-like materials in the product are polycrystalline $Ni(OH)_2{\cdot}0.75H_2O$. HRTEM image (Fig. 3(f)) shows that the crystallinity of $Ni(OH)_2{\cdot}0.75H_2O$ nanosheets is relatively weak. No diffraction peaks of $Ni(OH)_2{\cdot}0.75H_2O$ were observed in the XRD pattern (Fig. S6(b))), which is attributed to the weak crystallinity of $Ni(OH)_2{\cdot}0.75H_2O$ or small amount of $Ni(OH)_2{\cdot}0.75H_2O$ presented in the product compared to MoO_3 nanorods. As the reaction time increased to 2 h, the height of the $Ni(OH)_2{\cdot}0.75H_2O$ nanosheets also increased to about 130 nm, as shown in Fig. 3(g) and (h). XRD pattern (Fig. S6(c)) shows that the product obtained at 90°C for 2 h are composed of $NiMoO_4{\cdot}xH_2O$, MoO_3 and $Ni(OH)_2{\cdot}0.75H_2O$, similar to the product obtained at 90°C for 5 h (Fig. S6(d)). The diffraction rings marked by yellow lines in the SAED taken from the basal plane of the nanosheets (Fig. 3(h) correspond to (101), (015) and (110) crystalline planes of $Ni(OH)_2{\cdot}0.75H_2O$, respectively, whereas the diffraction dots marked by the green lines correspond to the crystalline planes of $NiMoO_4{\cdot}xH_2O$ with the lattice distances of 0.322 and 0.175 nm, respectively. With the further increase in the reaction time, the nanosheets will further grow and the regions of void spaces will gradually be enlarged (step 3 in Scheme 1), and finally the interesting 3D nanostructures will be obtained, as shown in Fig. 1(a). During the whole process, the length of the MoO_3 nanorods was gradually decreased due to alkali etching. It should be noted that the weak alkali etching is very important for the growth of the interesting 3D nanostructures. In the ethanol system, the concentration of OH^- ions is low, leading to very small numbers of the defect sites formed on the surfaces of the MoO_3 nanorods by the alkali etching. In the case, the nanosheets will not grow on the surfaces of the MoO_3 nanorods, as shown in Fig. 2(a). If nickel acetate was replaced with nickel nitrate or nickel dichloride, the same results were also obtained even in the ethanol/water system, as shown in Fig. 4(a) and 4(b). This further supports the conclusion above. However, in the water system, the concentration of OH^- ions is increased significantly. In this case, MoO_3 nanorods will be severely etched and small amount of products would be obtained, as shown in Fig. 2(b – d).

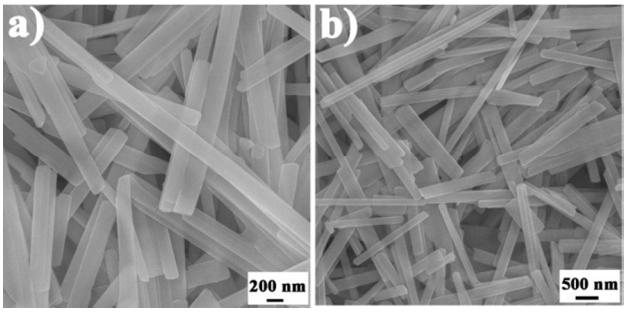

Fig. 4 a) and (b) SEM images of the products obtained as nickel acetate were replaced with nickel nitrate and nickel dichloride in the ethanol/water system, respectively.

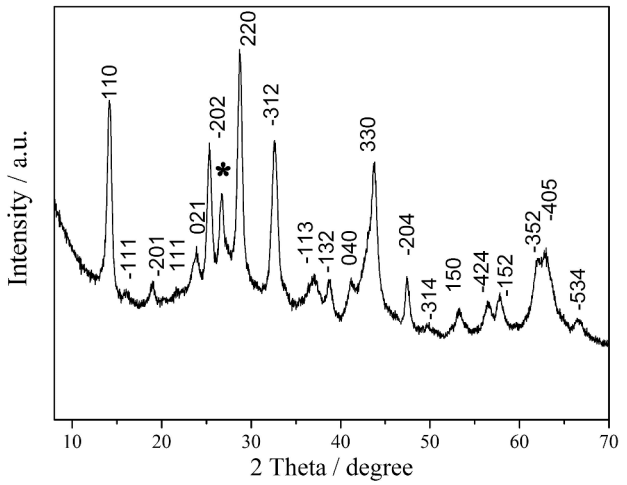

Fig. 5 XRD pattern of the hierarchical nanosheet-based $NiMoO_4$ nanotubes

In our previous work, we demonstrated that $Fe(OH)_3$@MoO_3 core/shell nanostructures could be converted into porous $Fe_2(MoO_4)_3$ nanorods by an in situ diffusion reaction.[13] The transformation mechanism is similar to one based on the nanoscale Kirkendall effect which usually used to fabricate hollow inorganic nanocrystals.[35] At a high temperature, MoO_3 diffused outward and reacted with Fe_2O_3, and then $Fe_2(MoO_4)_3$ gradually formed. Because MoO_3 diffused outward faster than Fe_2O_3 did inward, the void spaces would be formed in the inner of the nanorods. In this work, we adopted a similar method to

transform the 3D $NiMoO_4$ precursors to hierarchical nanosheet-based $NiMoO_4$ nanotubes. Fig. 5 shows a XRD pattern of the hierarchical nanosheet-based $NiMoO_4$ nanotubes. All diffraction peaks marked with Miller indices in the pattern can be indexed to monoclinic $NiMoO_4$ (JCPDS, no. 86−0361, cell parameters: a = 9.566 Å, b = 8.734 Å, c =7.649 Å, β = 114.22°). No significant peaks from NiO and MoO_3 were detected by the XRD measurement, suggesting that the precursors are fully converted into $NiMoO_4$ by the in situ diffusion reaction, $Ni(OH)_2{\cdot}0.75H_2O + MoO_3 \rightarrow NiMoO_4 + 1.75H_2O$. In addition, one unkwon peak marked by "*" was also observed, which needs to be further studied.

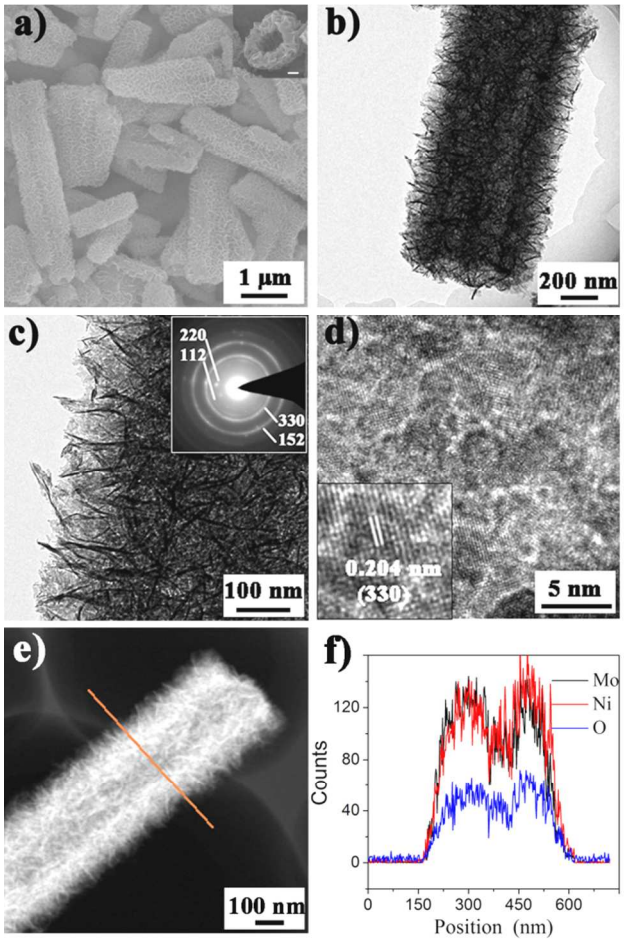

Fig. 6 Structural characterization of the hierarchical nanosheet-based $NiMoO_4$ nanotubes. a) SEM image, the inset showing the tubular characteristic of the products, the scale bar: 100 nm, b, c) TEM images, the inset showing SAED pattern, d) HRTEM image, the scale bar in the inset: 2 nm, e) ADF STEM image, and f) Line-scan EELS.

The morphology and the structure of the hierarchical nanosheet-based $NiMoO_4$ nanotubes were characterized by SEM and TEM analyses. SEM observations (Fig. 6(a)) show that the nanotubes have similar shape to that of the 3D precursors. Due to the in situ diffusion reaction, the region of void spaces along axial direction for the products is further enlarged compared to the precursors, as shown in the inset in Fig. 6(a). The tubular characteristic of the product is further confirmed by TEM analyses (Fig. 6(b)). The TEM analyses (Fig. 6(c)) also demonstrate that the thickness of the nanosheets grown outward is less than 10 nm. SAED pattern (the inset in Fig. 6(c)) reveals a polycrystalline nature of the hierarchical nanosheet-based $NiMoO_4$ nanotubes. The lattice distance marked in the inset in Fig. 6(d) is about 0.204 nm, corresponding to (330) crystal plane of monoclinic $NiMoO_4$. There are small many white regions in the HRTEM image (Fig. 6(d)) taken from the basal plane of the nanosheets, indicating a porous nature of the nanosheets. ADF STEM and line-scan EELS analyses (Fig. 6(e) and 6(f)) reveal that the Mo, Ni, and O distribute at the whole region of the products, and their quantities are much higher in the external region than in the inner one, also demonstrating that the products possess the tubular character.

The surface electronic state and composition of the hierarchical nanosheet-based $NiMoO_4$ nanotubes were investigated by XPS analysis. The survey XPS spectrum indicates that the nanotubes contain Ni, Mo, and O elements, as shown in the Supplementary, Fig. S7(a). † Fig. S7(b) shows a high-resolution Mo 3d spectrum. Deconvoluted Mo 3d doublet peaks at 232.1 and 235.4 eV suggest that molybdenum is solely in the state of Mo^{6+}.[36] † Fig. S7(c) shows a high-resolution Ni 2p spectrum, in which two peaks at 855.4 and 873.0 eV corresponds to Ni 2p3/2 and Ni 2p1/2, respectively.[37] † Thus, Mo^{6+} as the only detected molybdenum species and Ni^{2+} as the only nickel species. The atom ratio of Mo to Ni is about 1:1.1, suggesting that the surface of hierarchical nanosheet-based $NiMoO_4$ nanotubes is Ni-rich slightly with respect to stoichiometric $NiMoO_4$.

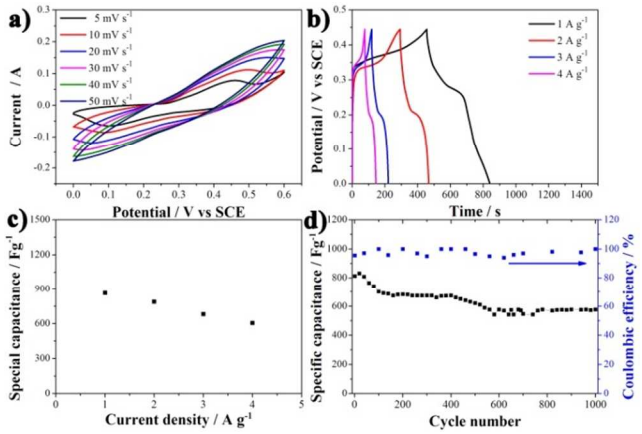

Fig. 7 Electrochemical characterizations of the hierarchical nanosheet-based $NiMoO_4$ nanotubes. a) CV curves, b) Galvanostatic discharge curves of the hierarchical nanosheet-based $NiMoO_4$ nanotube electrode at various discharge current densities, c) Specific capacitance of the hierarchical nanosheet-based $NiMoO_4$ nanotube electrode at various discharge current densities, and d) Cycling stability **and Coulombic efficiency** of the hierarchical nanosheet-based $NiMoO_4$ nanotube electrode at a current density of 1 A g^{-1}.

Fig. 7(a) shows the cyclic voltammogram (CV) curves of the hierarchical nanosheet-based $NiMoO_4$ nanotubes at different scan rates. A pair of redox peaks is observed in each curves suggesting that the measured capacitance is mainly based on the pseudocapacitive mechanism. On one hand, the intensities of the redox peaks increase with the scan rate; on the other hand, the cahodic peak shifted towards positive potential, while the cathodic peak shifted towards negative potential. This further confirms the psecudocapacitive behavior of the hierarchical nanotubes. Furthermore, even at a high scan rate (50 mV s^{-1}), the

redox peaks are still evident, suggesting that the hierarchical nanosheet-based $NiMoO_4$ nanotubes are stable as electrode for ECs and exhibit good rate capability.

In order to further understand the electrochemical performances of the hierarchical nanosheet-based $NiMoO_4$ nanotubes, we measured the static charge/discharge curves at various current densities at room temperature, as shown Fig. 7(b). The specific capacitance was calculated by the equation, $C_s = i\Delta t/(m\Delta V)$, where Cs (F/g) is the specific capacitance, i (A) is the discharge current, Δt (s) is the discharge time, m (g) is the weight of the active materials, ΔV (V) is the voltage interval of the discharge. As shown in Fig. 7(c), the calculated specific capacitances for the hierarchical nanotubes are 864, 788, 682, and 605 F g^{-1} at 1, 2, 3, 4 A g^{-1}, respectively. Compared with other metal molybdate such as $CoMoO_4$ (62.8 F g^{-1} at 1 A g^{-1}), $MnMoO_4$ (9.7 F g^{-1} at 1 A g^{-1}) and $MnMoO_4$ (187.1 F g^{-1} at 1 A g^{-1}) [16], the hierarchical nanosheet-based $NiMoO_4$ nanotubes exhibited superior electrochemical performances. Furthermore, the hierarchical nanotubes exhibited relatively good cycling stability even at 1 A g^{-1}. As shown in Fig. 7(d), after 1000 cycles, the capacitance retentions is still about 71%. In addition, the Coulmbic efficiency during the whole cycles is in range of 95 – 100 %, as shown in Fig. 7(d).

The good electrochemical performances of the hierarchical nanosheet-based $NiMoO_4$ nanotubes may be related to the following factors. (i) The hierarchical nanosheet-based $NiMoO_4$ nanotubes have a very high Brunauer−Emmet−Teller (BET) surface area of 128.5 m^2 g^{-1} (Fig. S8(a)), significantly higher than those of other metal molybdate nanostructures ($MnMoO_4$ nanorods[24]: 15 m^2 g^{-1}; $CoMoO_4$ nanorods[24]: 25 m^2 g^{-1}; 3D $MnMoO_4$/$CoMoO_4$ heteronanostructures[15]: 54.06 m^2 g^{-1}). † Such higher BET surface area allows the inner active sites of the electrode can be fully contacted with electrolyte. (ii) The high capacitance of the hierarchical nanotubes is attributed to their unique microstructures, i. e., composed of highly ordered nanosheets with an ultrathin thickness. On one hand, self-aggregation of the hierarchical nanotubes is greatly impeded; on the other hand, such microstructures can enhance the kinetics of ion and electron transport at the electrode-electrolyte interfaces and inside the electrodes. (iii) The hierarchical nanosheets grown on the $NiMoO_4$ nanotubes are of porous characteristic, as shown in Fig. 6(d). In addition, the average pore diameter is 11.8 nm (Fig. S8(b)), calculated from the desorption branch of the nitrogen isotherm obtaining using the Barret–Joyner–Halenda (BJH) method, and the corresponding BJH desorption cumulative volume is 0.52 cm^3 g^{-1}. † The porous characteristic and high pore volume make the eletrolyte diffusion in/outward electrode materials easily, which is favor of the improvement of the electrochemical performances of the hierarchical nanosheet-based $NiMoO_4$ nanotubes.

Conclusions

In summary, a facile method was developed to fabricate hierarchical nanosheet-based $NiMoO_4$ nanotubes with a high surface area of 128.5 m g^{-1}. The tubular character, highly ordered nanosheets with an ultrathin thickness, and high surface area resulted in excellent electrochemical performance of the nanotubes. As applied in ECs, the specific capacitance of the hierarchical nanotubes is up to 864 F g^{-1} at a current density of 1 A g^{-1}, and 71% of the initial capacitance after 1000 cycles was retained. Our results demonstrate that the hierarchical nanosheet-based $NiMoO_4$ nanotubes are very promising for applications in energy storage and other electrochemical devices. In addition, the strategy presented here could be expended as a general method to synthesize other kinds of metal molybdate nanotubes by rational designation in nanoscale.

Acknowledgements

We thank the National Natural Science Foundation of China (Grant Nos. 51272050 and 21271053), the Innovation Foundation of Harbin City (2012RFXXG096), and also the 111 project (B13015) of Ministry Education of China to the Harbin Engineering University.

Notes and references

[a] *Key Laboratory of In-Fiber Intregrated Optics, Ministry of Education, and College of Science, Harbin Engineering University, Harbin 150001, China. Fax: 86-451-82519754; Tel: 86-451-82519754; E-mail: chenyujin@hrbeu.edu.cn*

[b] *College of Materials Science and Chemical Engineering, Harbin Engineering University, Harbin, 150001, China.*

E-mail: *gaopeng@hrbeu.edu.cn*, and *yangpiaoping@hrbeu.edu.cn*

† Electronic Supplementary Information (ESI) available: [SEM and TEM images of MoO_3 nanorods, XRD and XPS measurements of 3D precursors, SEM image of the products without MoO_3 in the reaction system, XRD patterns of the samples obtained at different reaction stages, XPS, Nitrogen adsorption and desorption isotherms and the corresponding pore-size distribution of the hierarchical nanosheet-based $NiMoO_4$ nanotubes]. See DOI: 10.1039/b000000x/

1 H. Adkins, W. R. Peterson, *J. Am. Chem. Soc.*, 1931, **53**, 1512.
2 A. P. V. Soares, M. F. Portela, *Catal. Rev.*, 2005, **47**, 125.
3 J. Shirakawa, K. Nakayama, M. Wakihara and U. Yoshiharu, *J. Phys. Chem. B*, 2007, **111**, 1424.
4 M. P. House, A. Carley, R.F. Echeverria-Valda,M. Bowker, *J. Phys. Chem. C*, 2008, **112** , 4333.
5 L. Wang, B. Peng, X. F. Guo, W. P. Ding and Y. Chen, *Chem. Commun.*, 2009 , **45** ,1565.
6 J. Polanams, A. D. Ray, R. K. Watt, *Inorg. Chem.*, 2005 ,**44** , 3203.
7 M. Kumar, R. Awasthi, A. S. K. Sinha and R. N. Singh, *Int. J. Hydrogen Energy.*, 2008, **33**, 4260.
8 M. Kumar, R. Awasthi, A. S. K. Sinha and R. N. Singh, *Int. J. Hydrogen Energy*., 2011 , **33**, 8831.
9 R. N. Sigh, Madhu, R. Awasthi, A. S. K. Sinha, *J. Solid Electrochem*, 2009, **13**, 1613.
10 H. M. AbdelDayem, M. A. Al-Omair, *Ind. Eng. Chem. Res.*, 2008, **47**, 1011.
11 L. M. Maderira, M. F. Portela, *Appl. Catal. A*, 2005, **271**, 179.
12 Y. J. Chen, F. N. Meng, C. Ma, Z. W. Yang, C. L. Zhu, Q. Y. Ouyang, P. Gao, J. Q. Li and C. W. Sun, *J. Mater. Chem*., 2012, **22**, 12900.
13 Y. J. Chen, X. M. Gao, X. P. Di, Q. Y. Ouyang, P. Gao, L. H. Qi, C. Y. Li, and C. L. Zhu, *ACS Appl. Mater. Interfaces,* 2013, **5**, 3267.
14 W. M. Sears, *Sens. Actuators B: Chem*., 2000,**67,** 161.
15 L. Q. Mai, F. Yang, Y. L. Zhao, X. Xu, L. Xu and Y. Z. Luo, *Nat. Commun.*, 2011, **2**, 381.
16 M. C. Liu, L. B. Kong, C. Lu, X. M. Li, Y. C. Luo and L. Kang, *Mater. Lett.*, 2013, **94**, 197.
17 X. F. Xia, W. Lei, Q. L. Hao, W. J. Wang and X. Wang, *Electrochim. Acta.*, 2013, **99**, 253.
18 K. K. Purushothaman, M. Cuba and G. Muralidharan, *Mater. Res. Bull.*, 2012, **47**, 3348.
19 M. C. Liu, L. B. Kong, C. Lu, X. J. Ma, X. M. Li, Y. C. Luo and L. Kang, *J. Mater. Chem. A*, 2013, **1**, 1380.

20 G. K. Veerasubramani, K. Krishnamoorthy, S. Radhakrishnan, N. -J. Kim and S. J. Kim, *Int. J. Hydrogen Energy*, 2014, **39**, 5186.

21 Z. Xu, Z. Li, X. Tan, C. M. B. Holt, L. Zhang, B. S. Amirkhiz and D. Mitlin, *RSC Adv*., 2012, **2**, 2753.

22 C. T. Cherian, M. V. Reddy, S. C. Haur and B. V. R. Chowdari, *ACS Appl. Mater. Interfaces*, 2013,**5**, 918.

23 W. Xiao, J. S. Chen, C. M. Li, R. Xu and X. W. Lou, *Chem. Mater.*, 2010, **22**, 746.

24 Y. Ding, Y. Wan, Y. L. Min, W. Zhang and S. H. Yu, *Inorg. Chem.*, 2008, **47**, 7813.

25 a) J. Zhao, Q. S. Wu and M. Wen, *J. Mater. Sci*., 2009, **44**, 6356.; **b) X. J. Cui, S. H. Yu, L. Li, L. Biao, H. Li, M. Mo and X. M. Liu, *Chem. Eur, J.*, 2004, 10, 218.; c) S. H. Yu, B. Liu, M. Mo, J. H. Huang, X. M. Liu, Y. T. Qian, *Adv. Funct. Mater.*, 2013, 13, 639.**

26 a) L. L. Zhang, X. S. Zhao, *Chem. Soc. Rev.*, 2009, **38**, 2520.; b) Z. –Y. Yu, L. –F, Chen, S. –H. Yu, *J. Mater. Chem. A*, 2014, **2**, 10889.

27 M. Winter, R. J. Brodd, *Chem. Rev.*, 2004, **104**, 4245.

28 P. Simon, Y. Gogotsi, *Nat. Mater.*, 2008, **7**, 845.

29 J. R. Miller, P. Simon, *Science*, 2008, **321**, 651.

30 C. C. Hu, K. H. Chang, M. C. Lin and Y. T. Wu, *Nano Lett*., 2012, **6**, 2690.

31 Z. S. Wu, D. W. Wang, W. Ren, J. Zhao, G. Zhou, F. Li and H. M. Cheng, *Adv. Funct. Mater.*, 2010, **20**, 3595.

32 L. Fang, Y. Y. Shu, A. Wang and T. Zhang, *J. Phys. Chem. C*, 2007, **111**, 2401.

33 Y. J. Chen, G. Xiao, T. S. Wang, F. Zhang, Y. Ma, P. Gao, C. L. Zhu, E. D. Zhang, Z. Xu and Q. H. Li, *Sens. Actuators B.*, 2011, **155**, 270.

34 Q. Wang, Z. Lei, Y. Chen, Q. Ouyang, P. Gao, L. Qi, C. Zhu and J. Zhang, *J. Mater. Chem. A*, 2013, **1**, 11795.

35 Y. Yin, R. M. Rioux, C. K. Erdonmez, S. Hughes, G. A. Somorjai and A. P. Alivisatos, *Science*, 2004, **304**, 711.

36 Y. Okamoto, T. Imanaka and S. Teranishi, *J. Catal.*, 1981, **85**, 3798.

37 J.W. Lee, T. Ahn, D. Soundararajan, J.M. Ko and J. D. Kim, *Chem. Commun.*, 2011, **47**, 6305

Hierarchical nanosheet-based $NiMoO_4$ nanotubes with a high surface area of 128.5 m^2 g^{-1}, composed of highly ordered ultrathin nanosheets with a thickness of less than 10 nm, were synthesized by a hydrothermal treatment and subsequent an in situ diffusion reaction method, exhibiting excellent electrochemical performances.